

# Dynamic and Quasistatic Trajectories in Quasifission Reactions and Particle Emission

V. P. Aleshin<sup>1</sup>, M. Centelles<sup>2</sup>, X. Viñas<sup>2</sup>, and N. G. Nicolis<sup>3</sup>

<sup>1</sup>Institute for Nuclear Research, Kiev, 252028, Ukraine

<sup>2</sup>Departament d'Estructura i Constituents de la Matèria, Facultat de Física, Universitat de Barcelona, Diagonal 647, E-08028 Barcelona, Spain

<sup>3</sup> Department of Physics, University of Ioannina, Ioannina 45110, Greece

## Abstract

We show that the quasifission paths predicted by the one-body dissipation dynamics, in the slowest phase of a binary reaction, follow a quasistatic path, which represents a sequence of states of thermal equilibrium at a fixed value of the deformation coordinate. This establishes the use of the statistical particle-evaporation model in the case of dynamical time-evolving systems. Pre- and post-scission multiplicities of neutrons and total multiplicities of protons and  $\alpha$  particles in fission reactions of  $^{63}\text{Cu}+^{92}\text{Mo}$ ,  $^{60}\text{Ni}+^{100}\text{Mo}$ ,  $^{63}\text{Cu}+^{100}\text{Mo}$  at 10 MeV/u and  $^{20}\text{Ne}+^{144,148,154}\text{Sm}$  at 20 MeV/u are reproduced reasonably well with statistical model calculations performed along dynamic trajectories whose slow stage (from the most compact configuration up to the point where the neck starts to develop) lasts some  $35 \times 10^{-21}$  s.

PACS numbers: 25.70.Gh, 24.75.+i, 25.70.Jj

## 1 Introduction

In the last years many experimental efforts have been devoted to the study of heavy-ion fission at beam energies below 10–20 MeV/u accompanied with the emission of light particles. Initial experiments involved the observation of fission fragments emitted in coincidence with neutrons [1,2,3] or charged-particles [4,5,6,7,8,9]. More recently, combined coincidence neutron and charged-particle data became available [10,11,12,13]. The most important result of these experiments consists in the estimation of fission times which appear to be  $10^3$ – $10^4$  times longer than the characteristic time of the single-particle motion. This fact implies that thermal equilibrium is being established over the intrinsic degrees of freedom at each value of the fission

coordinate  $Q$  and validates the use of the Rayleigh dissipative function technique to treat the coupling of  $Q$  with the particle degrees of freedom [14].

Heavy-ion fission reactions accompanied by particle emission are used as a testing ground of the dissipation mechanisms of large-scale collective motion in hot nuclei (for a review see Refs. [15,16]). The main reason is that this process is simpler than other types of deep-inelastic collisions. The simplicity originates from the fact that fission is not sensitive to the fusion stage of a binary reaction whose understanding is far from clear.

When mass and projectile energy increase, the possibility to isolate the ground-state to scission-point motion becomes problematic because of the increasing contribution of quasifission, a fission-like process occurring at angular momenta  $J$  exceeding some value  $J_0$  where the fission barrier disappears. Quasifission in a clear cut sense has been observed in very heavy systems [17] which do not have a fission barrier even at  $J = 0 \hbar$ . These experiments provided a motivation for the creation of the code HICOL which proved to be capable of reproducing the general features of the process [18].

The Rayleigh function used in HICOL is built within the one-body dissipation model, proposed in Ref. [19]. It combines the wall formula in the mononuclear regime with an improved version of the so-called ‘completed window formula’ [20] in the dinuclear stage. Calculations show that quasifission originates from the fact that the potential of the composite system for  $J \approx J_0$  is very flat. Combined with strong friction this gives the system enough time to thermalize the relative velocity of the colliding nuclei and to relax the mass-asymmetry mode.

In medium mass reaction systems, a quasifission configuration can execute several rotations before scission, so that it is impossible to disentangle quasifission from fusion-fission by using fragment angular distributions as in heavier systems. Moreover, due to decreasing in angular momentum caused by the emission of few particles, a pocket can emerge in the initially flat potential, and a quasifission trajectory will go over into a fusion-fission one.

The introduction of quasifission trajectories to fission-evaporation routines is not an easy task. It requires answers on some principal questions. For example, in the fission case it is assumed [21] that, for all  $J$  within the fusion-fission angular momentum window, the system moves along the bottom of the fission valley of a non-rotating nucleus. Thus a question arises on whether the quasifission trajectories go along this path. Another related question is whether the evaporation model is applicable for particle emission along the quasifission trajectories.

The main purpose of the present work is to elucidate these questions. As a result we shall get a better perspective for a uniform description of fusion-fission and quasifission reactions accompanied by particle emission. To illustrate this opportunity, we test the compatibility of the charged particle clock with the neutron clock in calculations which effectively account for fusion-fission and quasifission trajectories. The study is performed in the  $A \approx 160$ ,  $E_x = 200\text{--}300$  MeV region, where a quite complete set of data on multiplicities of fission-associated light particles is available [10,12].

The paper is organized as follows. In Sect. 2 we define the quasistatic path and in Sect. 3 we introduce the geometrical quantities needed to characterize the quasistatic and dynamic configurations of the system. These quantities facilitate the comparison between the dynamic and quasistatic paths in Sect. 4. In Sect. 5 we perform Monte Carlo simulations of light-particle evaporation along dynamic trajectories and compare the results with available experimental data. Our conclusions are drawn in the last section.

## 2 The Quasistatic Path

The fundamental quantity in the construction of fission models is the total energy  $\tilde{E}\{\rho\}$  of the nucleus expressed as a functional of the spatial nucleon density  $\rho$ . The definition of this functional and its general properties are well documented (e.g., see Refs. [22,23,24,25]). Given  $\tilde{E}\{\rho\}$  one can use the equations

$$\frac{\delta\tilde{E}\{\rho\}}{\delta\rho} = 0, \quad \int \rho(\mathbf{r})d\mathbf{r} = A, \quad (1)$$

where  $\delta/\delta\rho$  is the functional derivative, to find the ground state and the saddle point densities  $\rho_{\text{gs}}$  and  $\rho_{\text{sd}}$ . The difference between the corresponding energies,  $\tilde{E}\{\rho_{\text{sd}}\} - \tilde{E}\{\rho_{\text{gs}}\}$ , gives the fission barrier height.

Since nuclei are leptodermous objects the terms ‘density’ and ‘shape’ are often used synonymously. As indicated first in Ref. [26], the so-called conditional equilibrium shapes may play an important role in nuclear dynamics. To define these shapes, one introduces a quantity  $Q$  characterizing the elongation of the nucleus.  $Q$  is a functional of the density and has the form

$$Q\{\rho\} = \int q(\mathbf{r})\rho(\mathbf{r})d\mathbf{r}, \quad (2)$$

where  $q(\mathbf{r})$  is a known function. The density  $\rho_{Q^*}$  of the conditional equilibrium shape is the solution of equations (1) in the class of densities  $\rho$  restricted

by the condition  $Q\{\rho\} = Q^*$  where  $Q^*$  is a constant. As pointed out in Ref. [26], the sequence of conditional equilibrium shapes may acquire a physical meaning, for instance it can describe the process of fission if  $Q$  is changing adiabatically compared to all other degrees of freedom. It was conjectured in Ref. [26] that the adiabaticity condition is likely to be satisfied in heavy systems where  $\tilde{E}\{\rho\}$  changes from the ground state to the saddle point by a few MeV only.

Nowadays, there is a strong evidence [16] that the dynamical equation for fission of hot nuclei should take into account the coupling of  $Q$  with the single-particle degrees of freedom, which causes a slowing down of the fission time scale to values exceeding the single-particle times by a few orders of magnitude. This allows one to assume that at each instant of time the single-particle degrees of freedom are in thermal equilibrium under the constraint of the known  $Q$  and the respective velocity  $\dot{Q}$ . Expressed in formal terms, this means that the entropy  $S$  of the system is maximal for the given constraints:

$$\frac{\delta S}{\delta \rho} = 0, \quad \int \rho(\mathbf{r}) d\mathbf{r} = A, \quad Q = Q^*, \quad \dot{Q} = \dot{Q}^*. \quad (3)$$

Equations (3) define a state of partial thermal equilibrium [14], or quasistatic state, for short.

Denoting the intrinsic excitation energy by  $E_x$  and using the Fermi gas formula for the entropy

$$S = 2\sqrt{a(E_x - \tilde{E}\{\rho\} + \tilde{E}\{\rho_{\text{gs}}\})}, \quad (4)$$

one can find the density  $\rho$  of the quasistatic state by looking for the conditional minimum of  $\tilde{E}$ . This is justified by the fact that the variation of the level density parameter  $a$  with shape is very smooth in comparison to that of  $\tilde{E}$  [27]. By changing  $Q^*$  one gets a sequence of quasistatic states which we call the quasistatic path. The fact that fission proceeds along the quasistatic path leads to significant simplifications in the formal description of this process. It also allows us to employ the statistical-model treatment of particle emission for the fissioning nucleus, because the single-particle degrees of freedom are in thermal equilibrium at each point of the quasistatic path.

Another process in which the quasistatic shapes can be useful is quasifission. The complete thermal equilibrium of the single-particle motion at a given shape may be reached during the reseparation stage of a quasifission

reaction if in the fusion stage the mass asymmetry mode and the relative velocity of the two colliding nuclei have relaxed. As a result, the quasifission trajectories in the reseparation stage will get on the quasistatic path. In practical terms, quasifission reactions are described by the one-body dissipation model of heavy ion collisions [18] implemented in the code HICOL, while the conditional equilibrium densities can be calculated in the framework of the extended Thomas–Fermi (ETF) model of non-spherical nuclei [27,28,29]. With these two models we wish to verify whether the dynamic trajectories in quasifission reactions follow the quasistatic path.

Our ETF calculations will be confined to mass and axially symmetric (about the  $z$  axis) prolate density distributions  $\rho(r, z)$  normalized to the mass number  $A$ , where  $r = \sqrt{x^2 + y^2}$  and  $x, y, z$  are the Cartesian coordinates. The energy density of the ETF model incorporates second-order gradient corrections with spin-orbit and effective mass terms [24], which are very important in describing the nuclear surface. We have performed the ETF calculations using a realistic Skyrme interaction, namely SkM\* [24]. From the ETF–SkM\* functional, we obtain fully self-consistent nuclear densities by solving the associated variational Euler–Lagrange equations in cylindrical coordinates, imposing a given value of the quadrupole moment  $Q_2$  [27,28,29]:

$$Q_2 = 2\pi \int_0^\infty \int_{-\infty}^\infty [2z^2 - r^2] \rho(r, z) r dr dz. \quad (5)$$

To account for nuclear rotation with angular momentum  $J$  we have included a rotational energy

$$E_{\text{rot}} = \frac{J^2}{2I} \quad (6)$$

to the ETF energy functional. Here,  $I$  is the rigid-body moment of inertia

$$I = \pi \int_0^\infty \int_{-\infty}^\infty [2z^2 + r^2] m \rho(r, z) r dr dz, \quad (7)$$

where  $m$  is the nucleon mass. It was assumed that the spin axis is directed perpendicular to the symmetry axis of the compound nucleus.

In HICOL the constant density approximation is used. Therefore, the nuclear density is completely determined by the profile function  $y(z)$  whose rotation about the symmetry axis  $z$  generates the nuclear surface. This poses difficulties in the comparison between dynamic and quasistatic densities, which can nevertheless be avoided by introducing some generalized characteristics of the nuclear densities.

### 3 Geometry of the Composite System

For the sake of comparison between dynamic and quasistatic paths we introduce the elongation coordinate  $D_{\text{mm}}$  and the neck coordinate  $R_{\text{neck}}$ . In axially symmetric nuclei these quantities are given by

$$D_{\text{mm}} = \frac{8\pi}{A} \int_0^\infty \int_0^\infty z \rho(r, z) r dr dz \quad (8)$$

and

$$R_{\text{neck}}^2 = \frac{2}{\rho_0} \int_0^\infty r \rho(r, z = 0) dr. \quad (9)$$

The elongation coordinate  $D_{\text{mm}}$  defines the distance between the centers of mass of the two halves of the nucleus. It was used by Strutinsky [26] as a constraint operator in the integro-differential equation for the profile function  $y(z)$  of leptodermous nuclei. Our definition (9) of the neck radius is obtained from the requirement that a nucleus with constant density  $\rho_0$  and a geometrical neck radius equal to  $R_{\text{neck}}$ , has the same number of particles in the cross section of its neck as the nucleus having the distributed density  $\rho$ . In the following,  $\rho_0$  in Eq. (9) will be identified with the one used in the code HICOL, namely  $\rho_0 = A/(\frac{4}{3}\pi R_0^3)$  where  $R_0 = 1.18 A^{1/3}$  fm. From Eqs. (8) and (9) one finds that for a spherical nucleus with a constant density  $\rho_0$ , the elongation  $D_{\text{mm}}$  is equal to  $\frac{3}{4}R_0$  and that the neck radius is  $R_{\text{neck}} = R_0$ .

In HICOL the profile function  $y(z)$  of the composite system is parameterized by two spheres smoothly connected by a second-order curve [30]. For these so-called Blocki shapes we define  $D_{\text{mm}}$  as the distance between the centers of mass of the two parts of the nucleus on both sides of a plane  $z = z_m$ . For  $z_m$  we take the mean value of the left and right matching points ( $z_m = 0$  for symmetric shapes). We identify  $R_{\text{neck}}$  of the Blocki profile with  $y(z_m)$ .

For mass symmetric shapes, the Blocki profile function reads

$$y^2(z) = \begin{cases} R_1^2 - (z + s/2)^2 & \text{for } -R_1 - s/2 \leq z \leq -z_1, \\ \alpha + \beta z^2 & \text{for } -z_1 \leq z \leq z_1, \\ R_1^2 - (z - s/2)^2 & \text{for } z_1 \leq z \leq s/2 + R_1. \end{cases} \quad (10)$$

Given the volume  $V_0$  of the nucleus, the parameters  $R_1$ ,  $z_1$ ,  $\alpha$  and  $\beta$  can be expressed in terms of the two collective degrees of freedom  $s$  and  $\sigma$ , where  $s$  is the distance between the centers of the spheres and

$$\sigma = \frac{V_0 - 8\pi R_1^3/3}{V_0} \quad (11)$$

is a measure of the constriction of the system.

Indeed, from Eq. (11) one obtains

$$R_1 = R_0 \left( \frac{1 - \sigma}{2} \right)^{1/3}, \quad (12)$$

where  $R_0$  is the radius of a spherical nucleus of volume  $V_0$ . If we equate the values of  $y(z)$  and its derivative on both sides of  $z = z_1$  and require that the total volume of the shape generated by  $y(z)$  equals  $V_0$ , we get

$$\alpha = R_1^2 + \frac{s}{2} \left( z_1 - \frac{s}{2} \right), \quad (13)$$

$$\beta = \frac{s}{2z_1} - 1, \quad (14)$$

$$z_1 = \frac{s}{2} \sqrt{1 - G}, \quad (15)$$

with

$$G = \frac{3}{s_0^2} - \frac{2}{s_0^3} \frac{1 + \sigma}{1 - \sigma}, \quad s_0 = \frac{s}{2R_1}. \quad (16)$$

For the Blocki shapes defined by Eq. (10), Eq. (8) yields

$$D_{\text{mm}} = \frac{3}{4R_0^3} \left\{ \frac{s^4}{48} [(1 - G)^{3/2} - 1] + \frac{1}{2}s^2 R_1^2 + \frac{4}{3}s R_1^3 + R_1^4 \right\}. \quad (17)$$

The value of  $R_{\text{neck}}^2$  coincides with  $y^2(0)$  and according to (10) is equal to  $\alpha$ . Thus, using Eqs. (13) and (15) we obtain

$$R_{\text{neck}}^2 = R_1^2 + \frac{s^2}{4} (\sqrt{1 - G} - 1). \quad (18)$$

Given  $R_0$ , Eqs. (17) and (18) together with Eqs. (12) and (16) allow one to express  $D_{\text{mm}}$  and  $R_{\text{neck}}$  in terms of  $s$  and  $\sigma$ .

In the following section, instead of the quadrupole moment, we use sometimes the moment of inertia as a constraint operator. It should be noted that for mass symmetric Blocki shapes these quantities can be found analytically:

$$Q_2 = 4\pi\rho_0 \left[ \frac{h(R_1 + h)^3}{4} \left( R_1 - \frac{h}{3} \right) - \frac{h}{6} (R_1^2 - h^2) z_1^2 - \frac{2}{15} h^2 z_1^3 + \frac{h z_1^4}{20} \right], \quad (19)$$

$$I = \pi m \rho_0 \left[ \frac{(R_1 + h)^3}{5} \left( \frac{8}{3} R_1^2 - \frac{R_1 h}{2} + \frac{h^2}{6} \right) + \frac{h}{3} (R_1^2 - h^2) z_1^2 + \frac{4}{15} h^2 z_1^3 + \frac{h z_1^4}{30} \right], \quad (20)$$

where  $h = s/2$ .

## 4 Dynamic and Quasistatic Paths

We now describe calculations performed in order to compare the dynamic trajectories with the quasistatic path. The calculations are carried out in the  $A \approx 160$  composite mass region, a region of continuous experimental efforts [1,2,4,5,7,8,9,10,12]. We start with the quasifission reaction following a  $^{60}\text{Ni} + ^{100}\text{Mo}$  collision at the beam energy  $E = 600$  MeV. In Fig. 1 we display the equidensity contour plots corresponding to the sequence of the ETF densities of conditional equilibrium for  $^{160}\text{Yb}$ , which represents the composite system in the collision. For each ETF density shown we have calculated the values of  $D_{\text{mm}}$  and  $R_{\text{neck}}$  by means of Eqs. (8) and (9). Inserting these  $D_{\text{mm}}$  and  $R_{\text{neck}}$  into Eqs. (17) and (18) and solving these equations with respect to  $s$  and  $\sigma$ , we can prescribe the Blocki profiles to the density distributions. From Fig. 1 one can see that such profiles are close, in general, to the  $\frac{1}{2}\rho_0$  curves of the ETF density distributions. In dinuclear configurations, however, the nascent fragments predicted by the ETF model are somewhat flattened in the  $r$  direction compared to the spherical form.

The densities shown in Fig. 1 were calculated accounting for the rotational energy with angular momentum  $J = 86 \hbar$ . The reasons for this choice of  $J$  will become clear in the next section. The calculations indicate that the quasistatic path depends weakly on the angular momentum. When one goes from  $J = 86 \hbar$  to  $J = 0 \hbar$  the quasistatic  $D_{\text{mm}}$  and  $R_{\text{neck}}$  change at most by 0.1 fm. In earlier ETF calculations [27] the energy  $\tilde{E}$  of the rotating nucleus along the quasistatic path was found to be very close to the sum of the energy of the non-rotating nucleus and the rotational energy computed with the moment of inertia of the latter. Moreover it was shown that the level density parameter is affected by rotation in a negligible amount if  $Q_2$  is fixed. These findings were interpreted as an indication that rotation has a small influence on the nuclear densities calculated in conditional equilibrium. Our direct calculations of shape parameters along the quasistatic path agree



with this conclusion.

We repeated the calculation of the  $J=86 \hbar$  quasistatic path with the constraint on the moment of inertia  $I$ , instead of  $Q_2$ . The path in the  $(D_{\text{mm}}, R_{\text{neck}})$  space turned out to be almost the same as the one we had found with the  $Q_2$  constraint: the differences in  $R_{\text{neck}}$  are no larger than  $\sim 1\%$ . Imposing the  $I$  constraint we not only obtain the same values for  $Q_2$  as with the  $Q_2$  constraint, but also find that the hexadecapole moment  $Q_4$  along the path is very similar. This means that the nuclear shapes must be equivalent with the  $I$  or  $Q_2$  constraint, as well.

The dynamic evolution of the shape of the  $^{60}\text{Ni}+^{100}\text{Mo}$  composite system (at  $J=86 \hbar$  and  $E=600$  MeV) computed with HICOL is shown in Fig. 2. In units of  $10^{-21}$  s, the first stage (when neck fills in) takes about 0.2, the mononucleus lives about 30 and the scission stage lasts about 5. At the end of the first stage the individual temperatures and angular velocities of the two nuclei, predicted by HICOL, become approximately equal. The time dependence of  $D_{\text{mm}}$  for different  $J$  values is depicted in Fig. 3, which shows a clear separation of the reactions into the fusion stage taking a fraction of  $10^{-21}$  s and a much longer reseparation stage. The duration time of the latter strongly changes from one  $J$  to another. For example, this time decreases from  $45 \times 10^{-21}$  s to  $15 \times 10^{-21}$  s when  $J$  increases from  $85 \hbar$  to  $100 \hbar$ .

Figure 4 shows on a  $(D_{\text{mm}}, R_{\text{neck}})$  plot how the dynamic trajectories with  $J=70, 75, 80, 85, 90, 95, 100, 105 \hbar$  are joining the quasistatic path determined for  $J=86 \hbar$ . The systems with  $J=70$  and  $75 \hbar$  terminate at the different points of this path (in the case of  $J=75 \hbar$  this happens after a slight rebound) while those with  $J=80-105 \hbar$ , having got on the quasistatic path shortly after rebound, proceed towards the scission point. In the vicinity of the scission point, they start to deviate progressively from the quasistatic path and yield a thinner neck for the same value of the elongation. We have found the dynamic paths, in the reseparation phase, to be rather stable against variations in the excitation energy and mass asymmetry. This follows from our dynamic calculations performed for the system  $^{60}\text{Ni}+^{100}\text{Mo}$  at the beam energy of 1200 MeV (Fig. 5), and for  $^{48}\text{Ca}$  on  $^{112}\text{Sn}$  at the beam energy of 480 MeV (Fig. 6).

Very small but regular deviations of the dynamic trajectories in their slowest phase from the quasistatic path are clearly observed in Figs. 4, 5 and 6. They are probably related to the fact that the dynamical and variational calculations involve different forces, and that in the ETF calculation we varied the whole density rather than just the nuclear profile. To verify

this assumption we calculated the quasistatic path for  $J = 86 \hbar$ , with a  $Q_2$  constraint, using the Yukawa-plus-exponential (YPE) forces [31] which are employed in the code HICOL. We looked for the conditional minimum of the system energy in the class of mass symmetric Blocki shapes. The result is displayed on Fig. 6 with square symbols. According to this figure, the dynamical paths in their slowest part practically coincide with the quasistatic YPE path.

It is interesting to note that the YPE quasistatic path predicts the onset of the scission stage at noticeably smaller values of  $D_{\text{mm}}$  than the Skyrme path. This is consistent with the fact that the saddle point configuration for the YPE force is more compact than for the SkM\* force. The deformation energy for the YPE force reaches its maximum (of about 27.8 MeV) at  $D_{\text{mm}} \sim 13.6$  fm, whereas the SkM\* energy reaches its maximum (about 25.1 MeV) at  $D_{\text{mm}} \sim 15.6$  fm. These deviations manifest the scale of errors introduced into variational calculations by simple parameterizations of nuclear shapes.

## 5 Particle Emission

In the preceding section we have shown that the dynamic trajectories in the reseparation stage closely follow the quasistatic path. This means that statistical models of particle emission can be applied in this stage. Below, we describe the technique for light-particle evaporation calculations along the slow phase, which will allow us to perform comparisons with experimental data.

Our procedure is based on a Monte Carlo simulation of particle decay chains in nuclei with a time-dependent shape. Given the excitation energy  $E_x$ , angular momentum  $J$ , the dynamic path and the time  $t_i$  for the beginning of the slow phase, we calculate the neutron ( $R_n$ ), proton ( $R_p$ ) and alpha particle ( $R_\alpha$ ) emission rates. We assume that the emission times  $t_e$  are distributed according to the exponential law  $\exp(-R_{\text{tot}}t_e)$ , where  $R_{\text{tot}} = R_n + R_p + R_\alpha$  is the total emission rate. A specific value of  $t_e$  is chosen using a generator of exponentially distributed random numbers. Having sampled the type of the emitted particle in proportion to the weights  $R_n/R_{\text{tot}}$ ,  $R_p/R_{\text{tot}}$  and  $R_\alpha/R_{\text{tot}}$ , we find the average excitation energy  $\bar{u}$  and root mean square angular momentum  $j_{\text{rms}} = \sqrt{j^2}$  of the corresponding daughter nucleus and take the latter as the new decaying nucleus. Assuming its shape to be the same as that of the parent nucleus at  $t_i + t_e$ , we simulate the next decay. The chain

of decays is terminated when the emission time exceeds the scission time of the nucleus and one proceeds to the next chain.

The pre-scission multiplicities  $M_\nu(J)$  are calculated as

$$M_\nu(J) = \frac{1}{\mathcal{N}} \sum_{i=1}^{\mathcal{N}} \mathcal{N}_\nu(i), \quad (21)$$

where  $\mathcal{N}_\nu(i)$  is the number of particles of type  $\nu$  ( $\nu = n, p, \alpha$ ) in a decay chain classified with the index  $i$ . Here,  $\mathcal{N}$  is the total number of decay chains for a given  $E_x$  and  $J$ . The explicit expressions for  $R_\nu$ ,  $\bar{u}$ ,  $\bar{j}^2$  are summarized in the Appendix. They were obtained in the framework of the classical statistical model of particle emission from non-spherical nuclei [32,33,34]. As shown in Ref. [35], the effects of the shape distortions on particle emission are treated by these formulas more rigorously than in heuristic models [36,37,38,39,40].

The input parameters of these formulas are the effective separation energies  $S_\nu^{\text{eff}}$  calculated including deformation energies [11], the level density parameter  $a$ , the height  $V_b$  and the radius  $R_b$  of the corresponding spherical barrier experienced by a particle. In the following calculations we employ the YPE values of  $S_\nu^{\text{eff}}$  for  $\nu = n, p, \alpha$ . In Fig. 7 the YPE values (solid lines) are compared with the ETF separation energies (dashed lines) on the quasistatic path in  $^{160}\text{Yb}$ . The ratio  $I/I_0$  of the deformed nucleus moment of inertia to that of the spherical one is used as the coordinate along the path.

The level density parameters  $a$  to be used later have been normalized at the spherical shape to the experimental value  $A/8.8 \text{ MeV}^{-1}$  obtained in Ref. [41]. The shape dependence of  $a$  has been calculated with the YPE forces following the prescription of Töke and Swiatecki [42]. As seen from Fig. 8, these  $a$  are close, by magnitude and shape dependence, to the  $a$  values from the ETF method. The dependence of  $V_b$  and  $R_b$  for  $n, p, \alpha$  on  $A$  and  $Z$  is parameterized in the same way as in Ref. [43]. The energy of the emitted neutron entering the corresponding  $R_b$  is replaced with its mean value  $\approx 2\tau$ , where  $\tau$  is the temperature of the daughter nucleus.

Recently, Lou *et al* [12] measured multiplicities of light particles in fission reactions of 10 MeV/u  $^{63}\text{Cu} + ^{92,100}\text{Mo}$  and 20 MeV/u  $^{20}\text{Ne} + ^{144,148,154}\text{Sm}$ . Our analysis of these data along with the data of Gonin *et al* [10] on  $^{60}\text{Ni} + ^{100}\text{Mo}$  is presented in Fig. 9 and Table 1. The measurements of multiplicities of  $n, p, \alpha$  in the latter work were performed at 9.2 and 10.9 MeV/u. The data we analyze are obtained by interpolation of the reported values to 10 MeV/u.

In the analysis we took into account that in these reaction systems an

appreciable amount of particles escape from the system during the *pre-equilibrium* stage. The measurements of linear-momentum transfer from projectile to target allowed Lou *et al* [12] to estimate that the mass and charge removed in this stage are  $(\delta A, \delta Z) = (8,4), (8,4), (6,3), (7,3)$  and  $(6,3)$  in the reactions  $^{63}\text{Cu}+^{92,100}\text{Mo}$  and  $^{20}\text{Ne}+^{144,148,154}\text{Sm}$ , respectively. Since experimental information on  $\delta A$  and  $\delta Z$  for the  $^{60}\text{Ni}+^{100}\text{Mo}$  system is not available, we used the values  $(\delta A, \delta Z) = (8,4)$  in the closest system,  $^{63}\text{Cu}+^{100}\text{Mo}$ . Lou *et al* [12] estimated the initial excitation energies of the equilibrated compound nuclei to be  $E_x = 227, 267, 289, 277$  and  $282$  MeV in the reactions of 10 MeV/u  $^{63}\text{Cu}+^{92,100}\text{Mo}$  and 20 MeV/u  $^{20}\text{Ne}+^{144,148,154}\text{Sm}$ , respectively. For the system of 10 MeV/u  $^{60}\text{Ni}+^{100}\text{Mo}$ , the linear interpolation between the excitation energies  $E_x = 251$  MeV and 293 MeV at 9.2 MeV/u and 10.9 MeV/u, respectively, obtained in Ref. [10], results in  $E_x = 271$  MeV.

This information on  $\delta A$ ,  $\delta Z$  and  $E_x$  was used as input in our *pre-scission* (equilibrium) multiplicity calculations. For all systems we used  $t_i = 1.1 \times 10^{-21}$  s and simulated  $\mathcal{N} = 200$  chains of decays. For each system we took only one HICOL trajectory, namely the trajectory whose contact-to-scission time  $t_{\text{cs}}$  is closest to  $40 \times 10^{-21}$  s. This condition results in  $J = 78, 86, 86, 85, 88, 93 \hbar$  in the reactions of  $^{63}\text{Cu}+^{92}\text{Mo}$ ,  $^{60}\text{Ni}+^{100}\text{Mo}$ ,  $^{63}\text{Cu}+^{100}\text{Mo}$  at 10 MeV/u and  $^{20}\text{Ne}+^{144,148,154}\text{Sm}$  at 20 MeV/u, respectively. The slow stage of the so-chosen (‘effective’) trajectories lasts some  $35 \times 10^{-21}$  s. This is consistent with the fission time scale of  $(35 \pm 15) \times 10^{-21}$  s deduced from a systematic study of pre-scission neutron multiplicities in 27 fission reactions induced by  $^{16,18}\text{O}$ ,  $^{40}\text{Ar}$  and  $^{64}\text{Ni}$  on targets with  $A = 141\text{--}238$  [3].

In the *post-scission* emission calculations, the thermal energy of the composite system at the moment of scission was shared between the complementary fragments in proportion to their masses. The spins of the fragments (about  $6 \hbar$  per fragment) were taken from HICOL output. To find  $A$  and  $Z$  of the primary fragments, we used the calculated n, p and  $\alpha$  pre-scission multiplicities (see Table 1). The calculated post-scission multiplicities of neutrons in all reactions but  $^{63}\text{Cu}+^{92}\text{Mo}$  are confined between the value of  $3.7 \pm 0.4$  measured in the system of  $^{16}\text{O}+^{154}\text{Sm}$  at  $E_x = 206$  MeV [3] and the value of  $4 \pm 1.1$  for  $^{60}\text{Ni}+^{100}\text{Mo}$  at 10 MeV/u which follows from interpolation of the 9.2 and 10.9 MeV/u data ( $3.6 \pm 1$  and  $4.5 \pm 1.2$ , respectively) of Ref. [10].

With accounting for post-scission emission, which is essential, in fact, only for neutrons, the total (equilibrium) multiplicities appear to be within the likely systematic uncertainties of the experimental points. The only noticeable exceptions are the total proton multiplicities in  $^{63}\text{Cu}+^{92}\text{Mo}$  and

$^{60}\text{Ni}+^{100}\text{Mo}$ , when the measured values are smaller than the calculated ones by factors of 1.6 and 2.1, respectively. With the exception of these two data points, the overall agreement of the calculations with the rest of the data signifies a consistency of the neutron with the charged particle clock. The low proton multiplicities in  $^{60}\text{Ni}+^{100}\text{Mo}$  reactions observed in Ref. [10] have motivated further experimental studies. In a recent work, Charity *et al* [44] studied the nearby system  $^{64}\text{Ni}+^{100}\text{Mo}$  at a similar excitation energy and found 2–3 times greater multiplicities of *fusion*-associated p and  $\alpha$  compared to those of Ref. [10].

It should be noted that no fitting parameters were used in our analysis. The employment of the transmission coefficients for p and  $\alpha$  from Ref. [45] would destroy the quality of the description by strongly enhancing the  $\alpha$  emission. For instance, the pre-scission multiplicities in the  $^{60}\text{Ni}+^{100}\text{Mo}$  system become 6.73, 2.29 and 1.81 for n, p and  $\alpha$ , respectively, instead of 7.27, 2.11 and 0.98 obtained with the transmission coefficients from Ref. [43].

## 6 Discussion and Conclusion

To shed more light on the role of quasifission trajectories in the reactions of our study, it is useful to estimate the fusion-fission  $J$ -window and compare it with available experimental information on the angular momenta, associated with the evaporation residue and fission cross sections. Nuclei emerging at the end of the evaporation cascades undergo fission if their angular momentum is confined between the angular momentum where the fission barrier height  $B_f(J)$  equals the neutron separation energy and the angular momentum where  $B_f(J)$  vanishes [46,47]. To reconstruct the corresponding  $J$ -window in the beginning of the evaporation cascades, one has to account for the angular momentum removed by pre-scission particles.

In the case of  $^{60}\text{Ni}+^{100}\text{Mo}$  at 10 MeV/u, we find that the fusion-fission  $J$ -window at the end of the evaporation cascades is 57–82  $\hbar$ , on the average. Light particles evaporated along the effective trajectory, remove on the average about 21  $\hbar$ . Therefore, we estimate the corresponding  $J$ -window in the beginning of the *equilibrium* emission stage, i.e. for  $^{152}\text{Dy}$ , to be 78–103  $\hbar$ . Since  $B_f(J)$  for  $^{152}\text{Dy}$  vanishes at 83  $\hbar$ , trajectories within this window, with the exception of those with  $J=78\text{--}83$   $\hbar$ , belong to quasifission.

It is interesting to note that the width of the so-defined  $J$ -window is close to the ‘total’ (fusion-fission plus quasifission)  $J$ -window widths in the closest

systems to ours, where data are available. A fission  $J$ -window of 70–103  $\hbar$  and 49–67  $\hbar$  is implied in studies of  $^{40}\text{Ar}+^{109}\text{Ag}$  at 8.4 MeV/u [48] and  $^{20}\text{Ne}+^{159}\text{Tb}$  at 16 MeV/u [49], respectively. Thus we may conclude that the majority of fission-evaporation reactions start on quasifission trajectories which after losing angular momentum end up on trajectories in the potential with a non-zero fission barrier.

To summarize, the present work was motivated by the desire to estimate the perspective for the inclusion of quasifission into fission-evaporation codes. Towards this aim we tested whether the quasifission trajectories, in the re-separation stage, follow the fission path. Our calculations were performed in the  $A \approx 160$  region at the bombarding energy of 10–20 MeV/u.

For the sake of comparison between different shapes (assumed to be axially symmetric) we use the two-dimensional space of the collective variables describing elongation and constriction. The elongation is characterized by the distance between the two halves of the nucleus. The constriction is described by the neck radius defined in a way applicable for distributed densities. In this collective space, we first check the sensitivity of the quasistatic path to the angular momentum of the system and to the form of the constraint operator. The quasistatic paths found for different angular momenta (including those exceeding the critical angular momentum for fission) are practically indistinguishable from the one with  $J=0 \hbar$ . The moment of inertia as a constraint operator was found to generate a sequence of shapes which coincides with the one obtained using the constraint on the quadrupole moment.

The same space of collective variables was used to compare the sequences of shapes predicted by the HICOL code at different values of the entrance-channel angular momentum. The parts of the quasifission trajectories corresponding to the slow stages of the evolution show the eventual convergence to the quasifission trajectory with the minimal  $J$ . This latter is found to follow closely the quasistatic path obtained with ETF model. This close coincidence of dynamic trajectories with the quasistatic path was found to occur in a wide range of bombarding energies and for quite different entrance-channel mass asymmetries.

Since the dynamics of quasifission reactions is well described by quasistatic paths, at least during the slowest phase, the statistical evaporation model can be applied for the description of particle emission from such systems. This follows from the fact that at each point of the quasistatic path the system reaches thermal equilibrium.

Using single *effective* dynamical trajectories whose slow stage lasts some

$35 \times 10^{-21}$  s, it was made possible to reproduce reasonably well experimental data on pre- and post-scission multiplicities of neutrons and total multiplicities of protons and  $\alpha$ -particles emitted from thermally equilibrated systems. This agreement was achieved without any *ad hoc* statistical model parameter adjustments and shows a consistency between the neutron and charged particle clock. The duration time of the slow stage of the employed dynamical trajectories was found consistent with the results of systematic studies.

## Acknowledgments

This research was supported by Grants No. PB98-1247 from the DGICYT (Spain), 1998SGR-00011 from the DGR (Catalonia), the General Secretariate of Research and Technology of the Ministry of Industry, Research and Technology of Greece ( $\Pi\epsilon\text{N}\epsilon\Delta$  '95 No. 696), and a NATO Fellowship Program for the Year 1996-97. Useful comments of Profs. W. Swiatecki and P. Schuck are greatly appreciated. We are thankful to Dr. Th. Keutgen for communicating us information on experimental data before publication.

## Appendix

In the following we outline the formalism we used for the calculation of decay rates for statistical particle emission from equilibrated compound nuclei. The excitation energy, angular momentum, deformation energy and moment of inertia of the parent nucleus are denoted as  $E_x$ ,  $J$ ,  $E_{\text{def}}$  and  $I_x$ , respectively. Given these quantities, the thermal energy of the parent nucleus is defined by

$$q_x = E_x - \frac{J^2}{2I_x} - E_{\text{def}}.$$

Its reduced level density is

$$\omega_x(q_x) = \frac{1}{t_x^A (I_x a_x)^{\frac{3}{2}}} \exp [2\sqrt{a_x q_x}],$$

where

$$t_x = \frac{3}{4a_x} + \sqrt{\left(\frac{3}{4a_x}\right)^2 + \frac{q_x}{a_x}},$$

and  $a_x$  is the level density parameter. Similar formulas are used for the reduced level density  $\omega(q)$  of the daughter nucleus with thermal energy  $q$ . Its moment of inertia and level density parameter are denoted by  $I$  and  $a$ .

The mass, spin and effective separation energy of the emitted particle are denoted as  $m_\nu$ ,  $s_\nu$  and  $S_\nu^{\text{eff}}$ , respectively. Let  $z_{\text{matter}}$  be half a length of matter distribution in the deformed shape, and let  $R_b$  and  $R_{\text{matter}}$  be the barrier radius and matter radius for the spherical shape. Then half a length of the figure generated by the barrier line is postulated to be

$$z_0 = z_{\text{matter}} + (R_b - R_{\text{matter}}).$$

Given the matter profile function  $y = y(z)$  and the Coulomb potential  $\Phi(z)$  along this profile, the barrier line  $\rho(z)$  and the potential barrier  $U(z)$  along this line were calculated from

$$\rho(z) = Ky \left( \frac{z}{K} \right), \quad U(z) = \frac{V_b}{\Phi_0} \Phi \left( \frac{z}{K} \right),$$

where  $K = z_0/z_{\text{matter}}$  is the scaling factor,  $V_b$  is the  $s$ -wave potential barrier in the spherical nucleus and  $\Phi_0$  is the Coulomb potential on the edge of the spherical matter distribution.

The key characteristics of the residual nucleus are its average thermal energy  $\bar{q}$  and temperature  $\tau$  corresponding to this thermal energy. These quantities are calculated from

$$\bar{q} \approx E_x - S_\nu^{\text{eff}} - E_{\text{def}} - \frac{J^2}{2I} - V_b,$$

$$\tau = \frac{2}{a} + \sqrt{\left(\frac{2}{a}\right)^2 + \frac{\bar{q}}{a}}.$$

With these definitions the particle emission rate is given by

$$R_\nu = \frac{2s_\nu + 1}{2\pi} m_\nu z_0^2 \tau^2 \frac{\omega(\bar{q})}{\omega_x(q_x)} \exp \left[ \frac{1}{\tau} \left( E_x - S_\nu^{\text{eff}} - E_{\text{def}} - \frac{J^2}{2I} - \bar{q} \right) \right] G(\tau, b),$$

where

$$G(\tau, b) = \int_{-1}^1 d\zeta \sqrt{\eta^2 + \eta^2 \left( \frac{d\eta}{d\zeta} \right)^2} \exp \left[ -\frac{U(\zeta z_0)}{\tau} + b\zeta^2 + \frac{1}{2}b\eta^2 \right] I_0 \left( \frac{1}{2}b\eta^2 \right),$$



$$b = b(\tau) = \frac{m_\nu z_0^2}{2\tau} \left( \frac{J}{I} \right)^2, \quad \eta = \eta(\zeta) = \frac{\rho(\zeta z_0)}{z_0},$$

and  $I_0(x)$  is a Bessel function of the first kind of imaginary argument.

The averaged square of the angular momentum of the daughter nucleus is

$$\overline{j^2} = J^2 - 4I\tau b \frac{d \ln G(\tau, b)}{db}.$$

Given this quantity and  $\bar{q}$ , the average excitation energy of the daughter nucleus reads

$$\bar{u} = \bar{q} + \frac{\overline{j^2}}{2I} + u_{\text{def}},$$

where  $u_{\text{def}}$  is the daughter nucleus deformation energy.

The above expressions give approximate values of  $R_\nu$ ,  $\overline{j^2}$  and  $\bar{u}$  because they use approximate values of  $\bar{q}$  and  $\tau$ . To correct these latter quantities we find a new value of  $\bar{q}$  using the formula

$$\bar{q} = E_x - S_\nu^{\text{eff}} - E_{\text{def}} - \frac{J^2}{2I} - 2\tau - \tau^2 \frac{d \ln G(\tau, b(\tau))}{d\tau}$$

at the initial value of  $\tau$  and insert it into the formula for  $\tau$ . This procedure was iterated until convergence of  $\tau$  was attained.

## References

- [1] A. Gavron, A. Gayer, J. Boissevain, H. C. Britt, T. C. Awes, J. R. Beene, B. Cheynis, D. Drain, R. L. Ferguson, F. E. Obenshain, F. Plasil, G. R. Young, G. A. Petitt, and C. Butler, Phys. Rev. C **35** (1987) 579
- [2] D. J. Hinde, D. Hilscher, and H. Rossner, Nucl. Phys. A **502** (1989) 497c
- [3] D. J. Hinde, D. Hilscher, H. Rossner, B. Gebauer, M. Lehmann and M. Wilpert, Phys. Rev. C **45** (1992) 1229
- [4] B. Lindl, A. Brucker, M. Bantel, H. Ho, R. Muffler, L. Schad, M. G. Trauth, and J. P. Wurm, Z. Phys. A **328** (1987) 85
- [5] R. Lacey, N. N. Ajitanand, M. Alexander, D. M. De Castro Rizzo, G. F. Peaslee, L. C. Vaz, M. Kaplan, M. Kildir, G. La Rana, D. J. Moses, W. E. Parker, D. Logan, M. Zisman, P. De Young, and L. Kowalski, Phys. Rev. C **37** (1988) 2540

- [6] F. Benrachi, B. Chambon, B. Cheynis, D. Drain, C. Pastor, H. Rossner, D. Hilscher, B. Gebauer, D. Husson, A. Giorni, D. Heuer, A. Lleres, P. Stassi and J. B. Viano, *Phys. Rev. C* **48** (1993) 2340
- [7] J. Boger, J. M. Alexander, R. A. Lacey, and A. Narayanan, *Phys. Rev. C* **49** (1994) 1587
- [8] W. E. Parker, M. Kaplan, D. J. Moses, J. M. Alexander, J. T. Boger, R. A. Lacey and D. M. de Castro Rizzo, *Nucl. Phys. A* **568** (1994) 633
- [9] W. E. Parker, M. Kaplan, D. J. Moses, J. M. Alexander, R. A. Lacey, D. M. de Castro Rizzo, J. Boger, A. Narayanan, G. F. Peaslee and D. G. Popescu, *Nucl. Phys. A* **594** (1995) 1
- [10] M. Gonin, L. Cooke, K. Hagel, Y. Lou, J. B. Natowitz, R. P. Schmitt, S. Shlomo, B. Srivastava, W. Turmel, H. Utsunomiya, R. Wada, G. Nardelli, G. Nebbia, G. Viesti, R. Zanon, B. Fornal, G. Prete, K. Niita, S. Hannuschke, P. Gonthier and B. Wilkins, *Phys. Rev. C* **42** (1990) 2125
- [11] J. P. Lestone, J. R. Leigh, J. O. Newton, D. J. Hinde, J. X. Wei, J. X. Chen, S. Elfstrom, M. Zielinska-Pfabe, *Nucl. Phys. A* **559** (1993) 277
- [12] Y. Lou, M. Gonin, R. Wada, K. Hagel, J. Li, B. Xiao, M. Gui, D. Utley, R. Tezkratt, L. Cooke, T. Botting, B. Hurst, D. O'Kelly, G. Mouchaty, R. P. Schmitt, W. Turmel, J. B. Natowitz, D. Fabris, G. Nebbia, G. Viesti, J. Ruiz, B. Burch, F. Gramegna, M. Poggi, G. Prete, M. E. Brandan and A. Menchaca-Rocha, *Nucl. Phys. A* **581** (1995) 373
- [13] W. H. Trzaska, J. Äystö, Z. Radivojevic, V. A. Rubchenya, I. D. Alk-hazov, S. V. Khlebnikov, A. V. Kuznetsov, A. Evsenin, V. G. Lyapin, O. I. Osetrov, G. P. Tiourin, D. N. Vakhtin, A. A. Alexandrov, Yu. E. Penionzhkevich, Yu. V. Pyatkov, Yu. G. Sobolev, M. Mutterer, J. von Kalben, and K. Brinkmann, *Acta Physica Slovaca* **49** (1999) 93
- [14] L. D. Landau and E. M. Lifshitz, *Statistical Physics. Part 1. Third Edition. Ch. XII Fluctuations.* Moscow: Nauka, 1976
- [15] Y. Abe, S. Ayik, P.-G. Reinhard, E. Suraud, *Phys. Rep.* **275** (1996) 49
- [16] P. Fröbrich and I. I. Gontchar, *Phys. Rep.* **292** (1998) 131
- [17] J. Töke, R. Bock, G. X. Dai, A. Gobbi, S. Gralla, K. D. Hildenbrand, J. Kuzminski, W. F. J. Müller, A. Olmi, H. Stelzer, B. B. Back and S. Bjørnholm, *Nucl. Phys. A* **440** (1985) 327
- [18] H. Feldmeier, *Rep. Prog. Phys.* **50** (1987) 915

- [19] J. Blocki, Y. Boneh, J. R. Nix, J. Randrup, M. Robel, A. J. Sierk and W. J. Swiatecki, *Ann. of Phys.* **113** (1978) 330
- [20] J. Randrup and W. J. Swiatecki, *Nucl. Phys. A* **429** (1984) 105
- [21] I. I. Gontchar, L. A. Litnevsky and P. Fröbrich, *Comp. Phys. Comm.* **107** (1997) 223
- [22] I. Zh. Petkov, M. V. Stoitsov, *Nuclear Density Functional Theory*, Clarendon Press, Oxford, 1991
- [23] P. Ring, P. Schuck, *The Nuclear Many-Body Problem*, Springer-Verlag, New York, Heidelberg, Berlin (1980)
- [24] M. Brack, C. Guet and H. B. Håkansson, *Phys. Rep.* **123** (1985) 275
- [25] M. Centelles, M. Pi, X. Viñas, F. Garcias, M. Barranco, *Nucl. Phys. A* **510** (1990) 397
- [26] V. M. Strutinsky, *JETP* **42** (1962) 1571; V. M. Strutinsky, N. Ya. Lyashchenko, N. A. Popov, *JETP* **43** (1962) 584; *Nucl. Phys.* **46** (1963) 639
- [27] F. Garcias, M. Barranco, J. Németh and C. Ngô, *Phys. Lett. B* **206** (1988) 177
- [28] F. Garcias, M. Barranco, J. Németh, C. Ngô and X. Viñas, *Nucl. Phys. A* **495** (1989) 169c; F. Garcias, M. Barranco, A. Faessler and N. Ohtsuka, *Z. Phys. A* **336** (1990) 31
- [29] M. Centelles, X. Viñas, M. Barranco, N. Ohtsuka, A. Faessler, D. T. Khoa and H. Müther, *Phys. Rev. C* **47** (1993) 1091
- [30] J. Blocki, Preprint (Institute for Nuclear Research, Swierk, Poland), 1980; J. Blocki, *J. de Phys. Colloq. C* **6** (1984) 489; J. Blocki, R. Planeta, J. Brzychczyk and K. Grotowski, *Z. Phys. A* **341** (1992) 307
- [31] H. J. Krappe, J. R. Nix and A. J. Sierk, *Phys. Rev. C* **20** (1979) 992; P. Möller and J. R. Nix, *Nucl. Phys. A* **361** (1981) 117
- [32] V. P. Aleshin, *J. Phys. G* **14** (1988) 339
- [33] V. P. Aleshin, *J. Phys. G* **16** (1990) 853
- [34] V. P. Aleshin, *J. Phys. G* **19** (1993) 307
- [35] V. P. Aleshin, *Nucl. Phys. A* **605** (1996) 120
- [36] M. Blann, *Phys. Rev. C* **21** (1980) 1770
- [37] Th. Dossing, Ph.D. Thesis (Copenhagen, NBA), 1978

- [38] N. N. Ajitanand, G. La Rana, R. Lacey, D. J. Moses, L. C. Vaz, G. F. Peaslee, D. M. De Castro Rizzo, M. Caplan and J. M. Alexander, *Phys. Rev. C* **34** (1986) 877
- [39] N. G. Nicolis, D. G. Sarantites, L. A. Adler, F. A. Dilmanian, K. Honkanen, Z. Majka, L. G. Sobotka, Z. Li, T. M. Semkow, J. R. Beene, M. L. Halbert, D. C. Hensley, J. B. Natowitz, R. P. Schmitt, D. Fabris, G. Nebbia and G. Mouchaty, *Phys. Rev. C* **41** (1990) 2118
- [40] K. Pomorski, J. Bartel, J. Richert, K. Dietrich, *Nucl. Phys. A* **605** (1996) 141
- [41] S. Henss, A. Ruckelshausen, R. D. Fischer, W. Kühn, V. Metag, R. Novotny, R. V. F. Janssens, T. L. Khoo, D. Habs, D. Schwalm, D. Freeman, G. Duchène, B. Haas, F. Haas, S. Hlavac and R. S. Simon, *Phys. Rev. Lett.* **60** (1988) 11
- [42] J. Töke and W. J. Swiatecki, *Nucl. Phys. A* **372** (1981) 141
- [43] M. Blann, *Phys. Rev. C* **21** (1980) 1770
- [44] R. J. Charity, M. Korolija, D. G. Sarantites, and L. G. Sobotka, *Phys. Rev. C* **56** (1997) 873
- [45] M. A. McMahan and J. M. Alexander, *Phys. Rev. C* **21** (1980) 1261
- [46] S. Cohen, F. Plasil, and W. J. Swiatecki, *Ann. Phys.* **82** (1974) 557
- [47] Y. Aritomo, T. Wada, M. Ohta, Y. Abe, *Phys. Rev. C* **59** (1999) 796
- [48] H. C. Britt, B. H. Erkkila, R. H. Stokes, H. H. Gutbrod, F. Plasil, R. L. Ferguson, and M. Blann, *Phys. Rev. C* **13** (1976) 1483
- [49] Th. Keutgen, J. Cabrera, Y. El Masri, C. Ghisalberty, I. Tilquin, L. Lebreton, A. Ninane, J. Lehmann, V. Roberfroid, L. Michel, R. Régimbart, J. B. Natowitz, K. Hagel, R. Wada, and R. J. Charity, 1999, *Nucl. Phys. A* **654** (1999) 878c

Table 1. Comparison between experimental and calculated light-particle multiplicities for the reaction systems studied in Refs. [10] and [12]. The neutron number  $N$  of the composite system after the pre-equilibrium emission stage is indicated. From left to right the systems are 10 MeV/u  $^{63}\text{Cu}+^{92}\text{Mo}$ ,  $^{60}\text{Ni}+^{100}\text{Mo}$ ,  $^{63}\text{Cu}+^{100}\text{Mo}$  and 20 MeV/u  $^{20}\text{Ne}+^{144,148,154}\text{Sm}$

$N$	80	86	88	89	92	99
$n^{\text{pre}}$	3.75	7.27	7.46	7.65	8.2	10.87
$n^{\text{post}}$	1.79	3.84	3.87	3.82	3.89	3.97
$n^{\text{tot}}$	5.54	11.11	11.33	11.47	12.09	14.84
$n^{\text{tot,exp}}$	6(1)	11.25(2.7)	10.9(1.5)	10.3(1.3)	12.2(1.6)	16.9(1.2)
$p^{\text{pre}}$	2.97	2.11	1.97	2.65	1.85	0.82
$p^{\text{post}}$	0.18	0.06	0.05	0.07	0.05	0.02
$p^{\text{tot}}$	3.15	2.17	2.02	2.72	1.9	0.84
$p^{\text{tot,exp}}$	2.02(0.3)	1.03(0.15)	1.6(0.3)	2.14(0.3)	1.83(0.5)	0.97(0.5)
$\alpha^{\text{pre}}$	1.17	0.98	0.93	1.24	1.	0.66
$\alpha^{\text{post}}$	0.03	0.02	0.01	0.02	0.01	0.01
$\alpha^{\text{tot}}$	1.2	1	0.94	1.26	1.01	0.66
$\alpha^{\text{tot,exp}}$	1(0.3)	0.77(0.11)	1.69(0.4)	1.3(0.3)	0.7(0.4)	0.63(0.4)

## Figure Captions

Fig. 1. Equidensity contours for  $^{160}\text{Yb}$  calculated by the ETF method at the indicated values of the quadrupole moment, with angular momentum  $J=86\hbar$ . From outside to inside the lines represent contours of constant density  $\rho = 0.1, 0.3, 0.5, 0.7, 0.9$  and  $1.1$ , in units of  $\rho_0$ . The dashed curves represent the Blocki profile with the parameters  $s$  and  $\sigma$  calculated in terms of  $D_{\text{mm}}$  and  $R_{\text{neck}}$  obtained from the corresponding ETF density distribution.

Fig. 2. Time evolution of the  $^{60}\text{Ni}+^{100}\text{Mo}$  system from the code HICOL at  $E = 600$  MeV and  $J=86\hbar$ . The time is indicated in units of  $10^{-21}$  s.

Fig. 3. Time dependence of  $D_{\text{mm}}$  for the reaction  $^{60}\text{Ni}+^{100}\text{Mo}$  at  $E = 600$  MeV and  $J=79-105\hbar$  predicted by the HICOL code.

Fig. 4. Dynamic (for  $J = 70, 75, 80, 85, 90, 95, 100, 105\hbar$ ) and quasistatic (for  $J=86\hbar$ ) paths in the  $^{60}\text{Ni}+^{100}\text{Mo}$  collision at 600 MeV are shown as solid and dashed lines, respectively. The spherical shape is shown as a cross. Numbers along the curves indicate the time in units of  $10^{-21}$  s for the dynamic path at  $J=86\hbar$ . The insert shows the final stage of the fusion trajectories with  $J=70\hbar$  and  $J=75\hbar$ .

Fig. 5. Dynamic paths (for  $J = 70, 75, 80, 85, 90, 95, 100, 105\hbar$ ) in the  $^{60}\text{Ni}+^{100}\text{Mo}$  collision at 1200 MeV are shown as solid lines. The quasistatic path for  $J=86\hbar$  is represented by the dashed line. The spherical shape is shown as a cross.

Fig. 6. Dynamic paths (for  $J=70, 75, 80, 85, 90, 95, 100, 105\hbar$ ) for the collision  $^{48}\text{Ca}+^{112}\text{Sn}$  at 480 MeV are shown as solid lines. The dashed line represents the quasistatic path corresponding to the self-consistent ETF variational calculation with the SkM\* force. The closed square symbols show the quasistatic path found for the YPE forces in the space of Blocki shapes.

Fig. 7. The effective separation energies of neutrons, protons and alpha particles along the quasistatic path in  $^{160}\text{Yb}$ . The solid lines show the calculation for the dynamic shapes with YPE forces. The dashed lines indicate the ETF effective separation energies.

Fig. 8. The level density parameter along the quasistatic path. The solid line represents the  $a$  values normalized to  $A/8.8\text{ MeV}^{-1}$  for the spherical shape with the Tōke-Swiatecki shape-dependent factor based on YPE forces. The dashed line indicates the ETF calculation.

Fig. 9. Equilibrium total multiplicities of neutrons, protons and alpha particles (pre-scission plus post-scission) as a function of the neutron num-

ber  $N$  of the emitting system (after the pre-equilibrium stage). Experimental data points from Refs. [12] and [10] are shown by filled squares and crosses, respectively. The short-dashed lines represent the calculated pre-scission (equilibrium) multiplicities. The solid lines show the total calculated multiplicities. In the top (neutron) panel, the open circles represent the total measured multiplicities accounting for pre-equilibrium emission [12]. From left to right the systems are 10 MeV/u  $^{63}\text{Cu}+^{92}\text{Mo}$ ,  $^{60}\text{Ni}+^{100}\text{Mo}$ ,  $^{63}\text{Cu}+^{100}\text{Mo}$  and 20 MeV/u  $^{20}\text{Ne}+^{144,148,154}\text{Sm}$ .

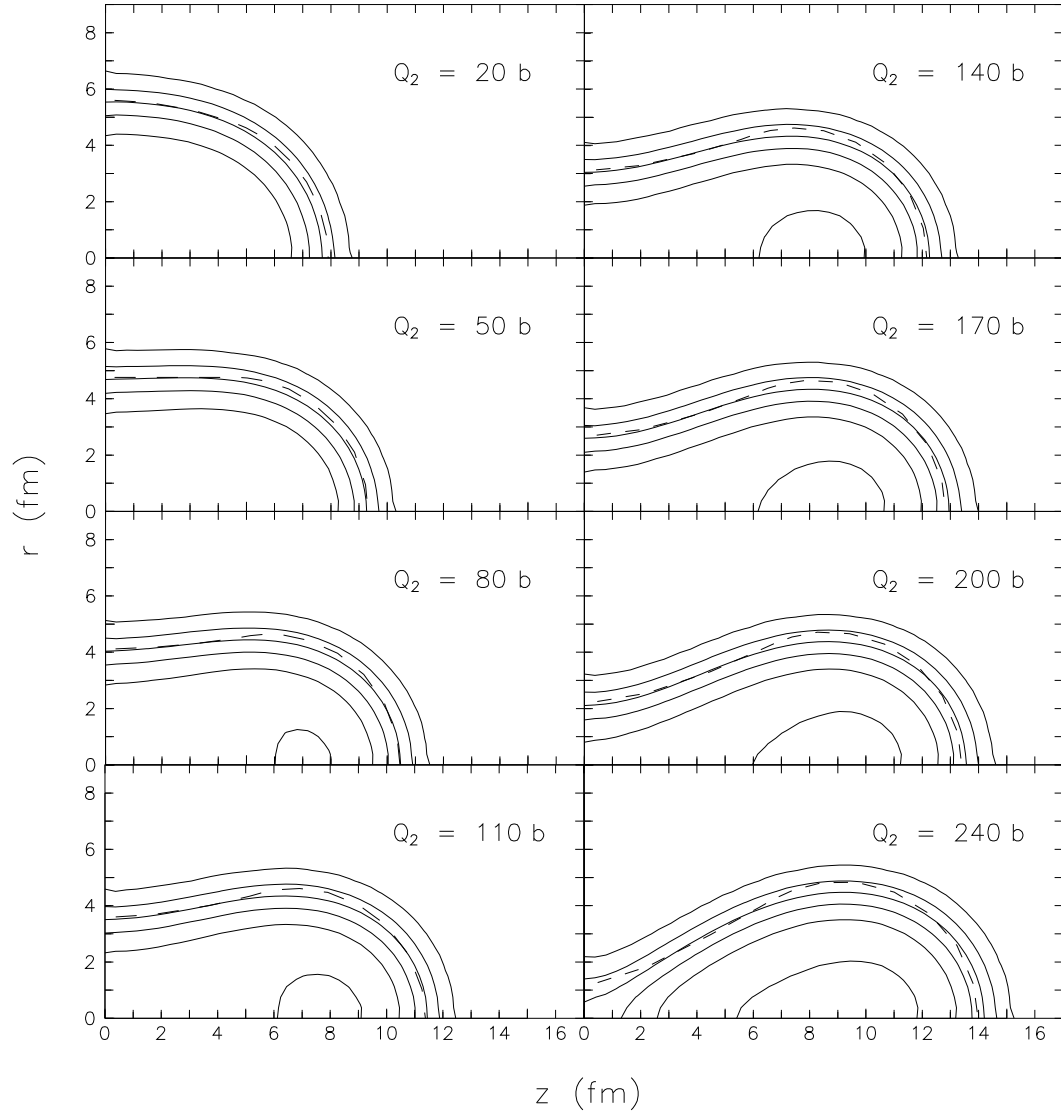


Figure 1



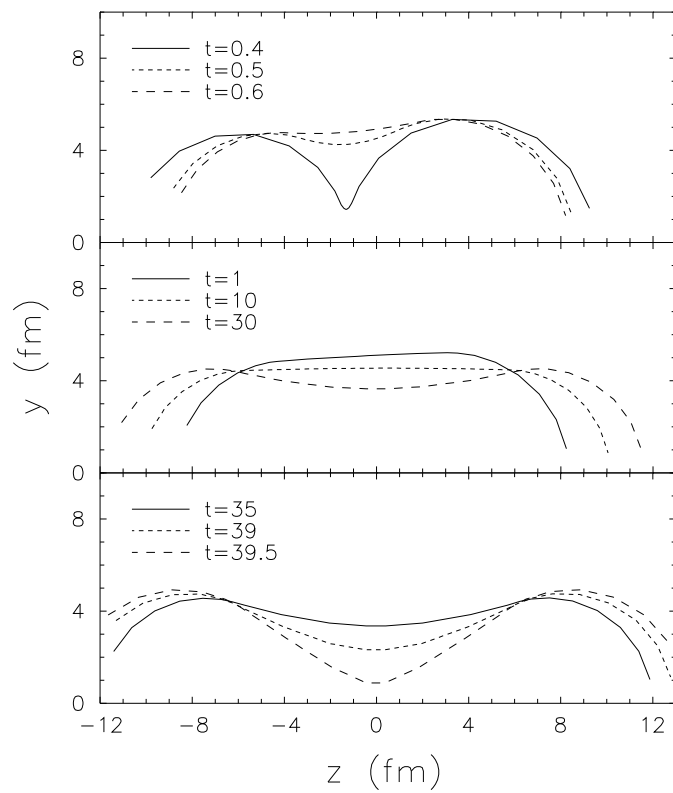


Figure 2

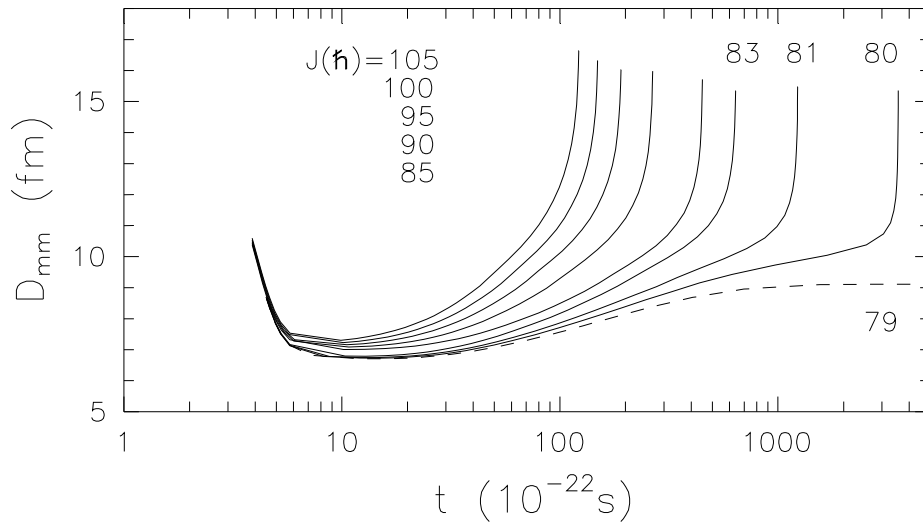


Figure 3

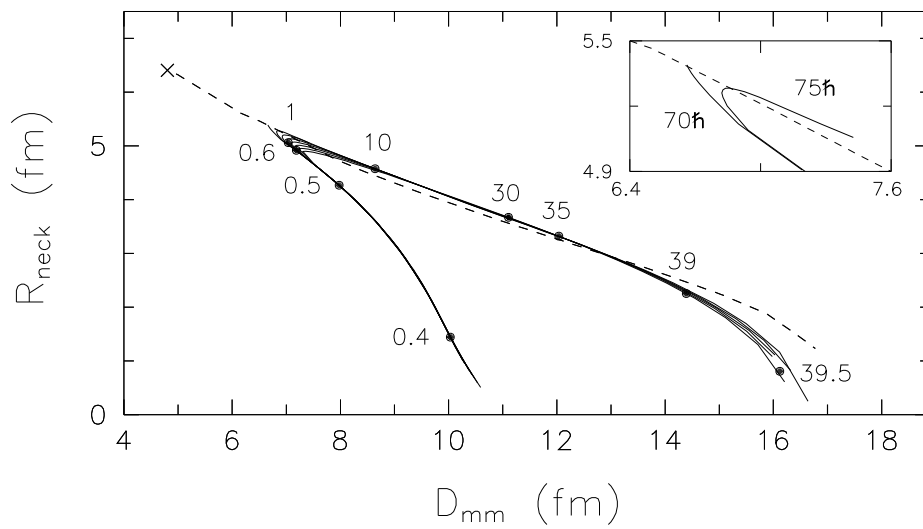


Figure 4

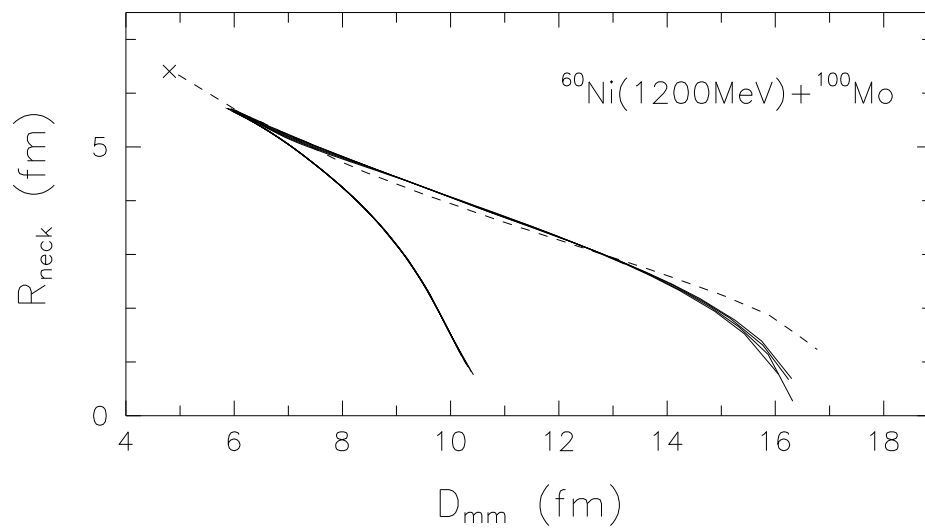


Figure 5

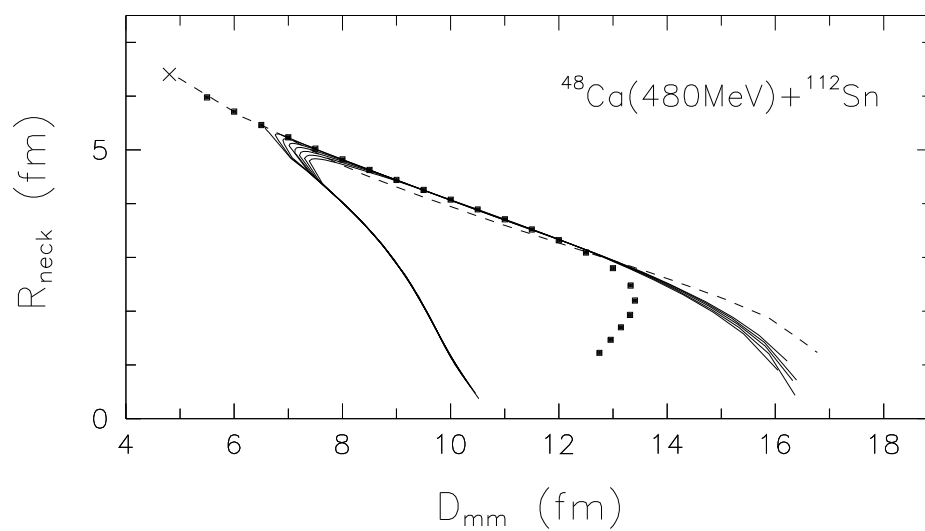


Figure 6

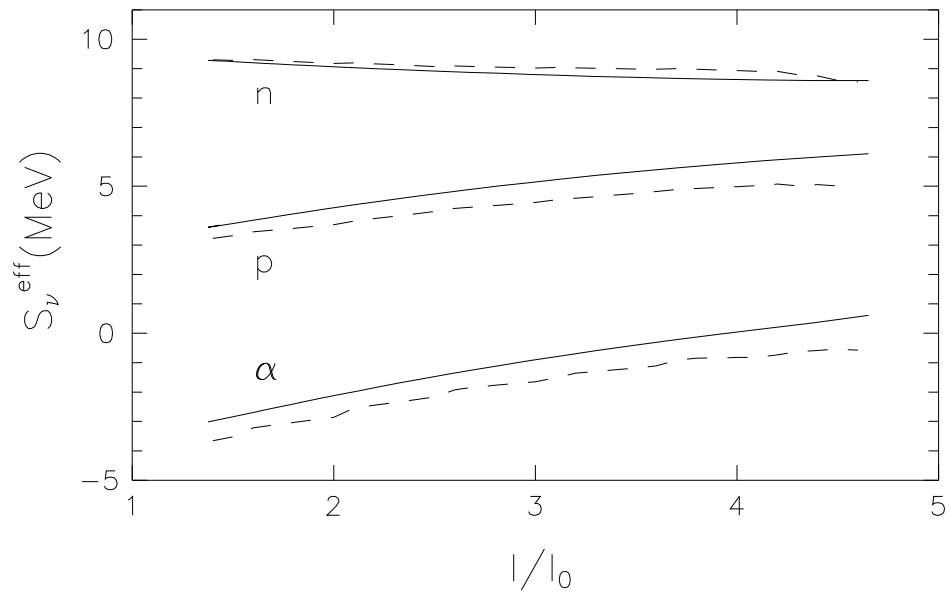


Figure 7

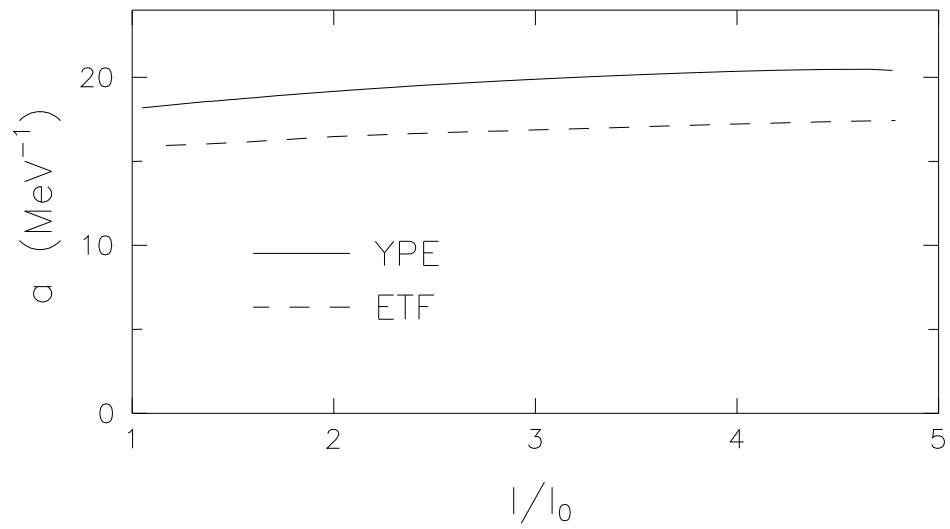


Figure 8

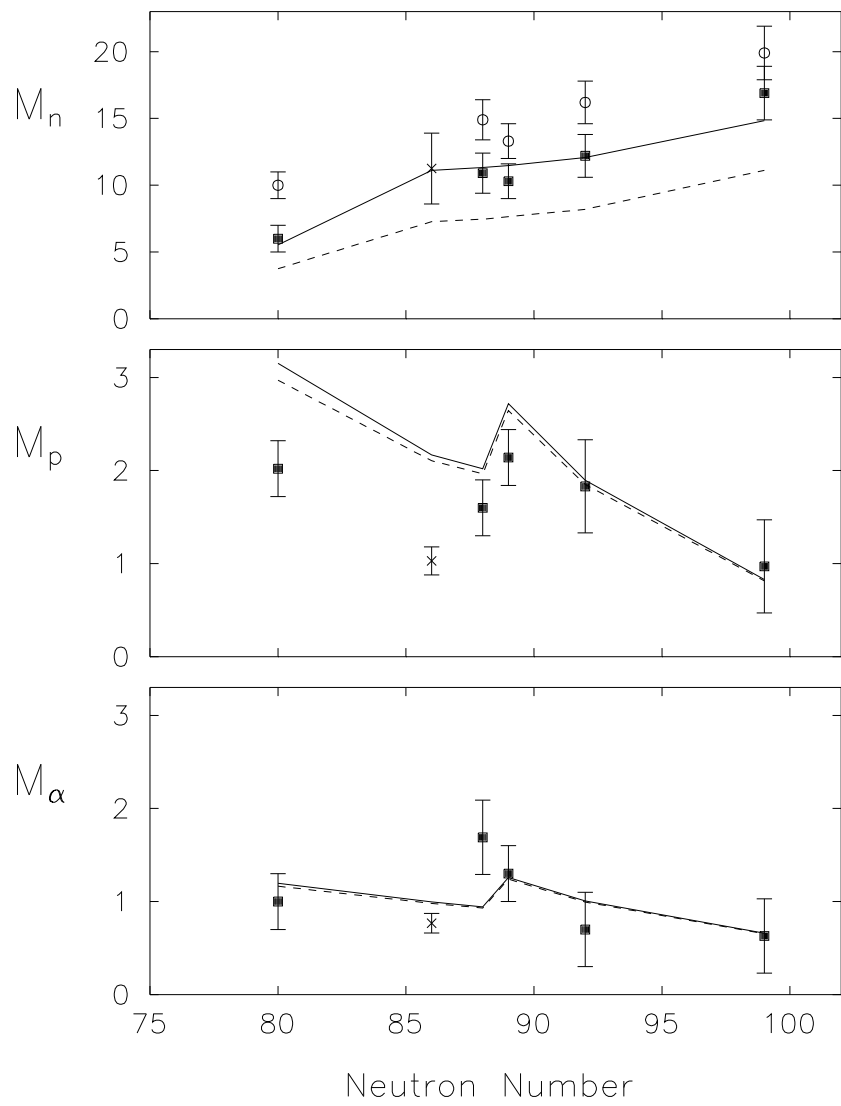


Figure 9